optica

Direct polarization measurement using a multiplexed Pancharatnam–Berry metahologram

Xueqian Zhang,[1,8] Shumin Yang,[2] Weisheng Yue,[3] Quan Xu,[1] ⊕ Chunxiu Tian,[4] Xixiang Zhang,[4] Eric Plum,[5] Shuang Zhang,[6] Jiaguang Han,[1,9] and Weili Zhang[1,7,*]

[1]*Center for Terahertz Waves and College of Precision Instrument and Optoelectronics Engineering,*
Tianjin University and the Key Laboratory of Optoelectronics Information and Technology (Ministry of Education), Tianjin 300072, China
[2]*Shanghai Synchrotron Radiation Facility, Shanghai 201204, China*
[3]*Institute of Optics and Electronics, Chinese Academy of Sciences, P.O. Box 350, Chengdu 610209, China*
[4]*Physical Science and Engineering Division, King Abdullah University of Science and Technology (KAUST), Thuwal 23955-6900, Saudi Arabia*
[5]*Optoelectronics Research Centre and Centre for Photonic Metamaterials, University of Southampton, Highfield, Southampton SO17 1BJ, UK*
[6]*School of Physics and Astronomy, University of Birmingham, Birmingham B15 2TT, UK*
[7]*School of Electrical and Computer Engineering, Oklahoma State University, Stillwater, Oklahoma 74078, USA*
[8]*e-mail: alearn1988@tju.edu.cn*
[9]*e-mail: jiaghan@tju.edu.cn*
*Corresponding author: weili.zhang@okstate.edu

Polarization, which represents the vector nature of electromagnetic waves, plays a fundamental role in optics. Fast, simple, and broadband polarization state characterization is required by applications such as polarization communication, polarimetry, and remote sensing. However, conventional polarization detection methods face great difficulty in determining the phase difference between orthogonal polarization states and often require a series of measurements. Here, we demonstrate how polarization-dependent holography enables direct polarization detection in a single measurement. Using a multiplexed Pancharatnam–Berry phase metasurface, we generate orthogonally polarized holograms that partially overlap with a spatially varying phase difference. Both amplitude and phase difference can be read from the holographic image in the circular polarization basis, facilitating the extraction of all Stokes parameters for polarized light. The metahologram detects polarization reliably at several near-infrared to visible wavelengths, and simulations predict broadband operation in the 580–940 nm spectral range. This method enables fast and compact polarization analyzing devices, e.g., for spectroscopy, sensing, and communications. © 2019 Optical Society of America under the terms of the OSA Open Access Publishing Agreement

https://doi.org/10.1364/OPTICA.6.001190

1. INTRODUCTION

Polarization is a fundamental property of electromagnetic waves that characterizes the trajectory of the oscillating electric field vector [1]. The polarization state determines how light interacts with anisotropic, chiral, and magnetized matter and, therefore, forms the basis of a diverse range of optical technologies. Accurately determining the state of polarization is essential in applications such as polarization spectroscopy, ellipsometry, sensing, imaging, communications, and quantum information detection [2–7]. However, direct polarization measurements are challenging due to lack of straightforward methods for probing the phase information. Conventional methods are usually indirect and require a series of intensity measurements to determine the polarization state, for example, the intensities of light after passing through a wave plate with different rotation angles [8], or the intensities of differently polarized components of the incident light that passes through special beam splitting components [9]. In both cases, bulky optical setups and precise adjustment of high-quality

optical components are typically required. A polarization state is fully characterized by measurements of both the intensities and relative phase difference of two orthogonal polarization states. Circular polarizations, i.e., left-handed circular polarization (LCP) and right-handed circular polarization (RCP), are often used as the orthogonal basis for describing polarizations. Thus, by detecting the chiral phase difference and chiral amplitude contrast between the LCP and RCP components of a light beam, one can determine its polarization state. An opportunity for direct polarization measurements arises from metasurfaces, which have drawn much attention for their ability to tailor interfacial phase profiles arbitrarily with subwavelength resolution [10].

Composed of two-dimensional plasmonic or dielectric phase-control elements, metasurfaces provide a flat and ultracompact platform for flexible wavefront engineering [11–13]. Metasurface applications include anomalous refraction/reflection [14–18], lensing [19–22], special beam generation [23–25], surface plasmon coupling [26–28], etc. Some functionalities of metasurfaces

can even go beyond those of conventional optical elements. Due to their well-controlled phase profiles, metasurfaces are particularly useful for holography for recording dense information [29–32]. By properly incorporating anisotropic element design or multiplexed methods, polarization-dependent holography has been demonstrated [33–41]. Recent metasurface holographic demonstrations generated images with exotic properties, such as multicolor holography [42], chiral-dependent holography [43–45], holography with large angle tolerance [46], vectorial holography [47], and active holography [48,49]. However, functional devices based on the generated holographic images of metaholograms are very scarce [50,51].

To date, there have been several nonholographic works on metasurface polarimeters using metagratings [52–57], which still rely on the traditional method of spatially splitting certain polarized beams to avoid direct phase measurements. Here, for the first time, we experimentally demonstrate a polarimeter based on a circular-polarization-dependent metahologram by utilizing the Pancharatnam–Berry (PB) phase concept in the near-infrared to visible spectral range. By carefully designing the intensity and phase difference distributions of holographic images generated by incident LCP and RCP, we resolve the chiral phase difference through the interference pattern between the generated images. Together with the simultaneously obtained chiral amplitude contrast from the images, we can identify the polarization state with a good level of accuracy in only a single, fast measurement of the holographic image. Besides, our method is also more compact than conventional methods, as only one linear polarizer is required to accomplish the polarization measurement. By exploiting the advantages of metaholograms, our method is not only straightforward, but also capable of operating over a broad spectral range.

2. HOLOGRAPHIC POLARIMETRY CONCEPT

Figure 1 illustrates the working mechanism of the metahologram for polarization analysis. The metasurface is designed by using the PB phase method to display different holographic images under

LCP and RCP illumination. As illustrated in Fig. 1(a) [Fig. 1(b)], incident LCP (RCP) results in generation of an image by transmitted RCP (LCP), where the image consists of a ring containing a circular disk within its upper (lower) half. The intensity distributions of both images are mirror-symmetric with respect to the x direction, and the two rings generated by LCP and RCP overlap. Both the rings and disks in the images are designed to have uniform intensity distributions. Without loss of generality, let us assume the rings have helical phase distributions with topological charges of –1 and +1 for LCP and RCP illumination, respectively, as illustrated by φ_{RL} and φ_{LR} in Figs. 1(c) and 1(d), respectively. Their zero phases both coincide with the +x direction in the interest of simplicity. Consequently, simultaneous LCP and RCP illumination will result in a helical phase difference distribution with a larger topological charge of –2 on the ring. If the LCP and RCP components of the incident light have an initial phase difference of $\varphi_L^{in} - \varphi_R^{in} = \Delta\varphi$, the zero point of the phase difference distribution will be located at azimuth angle $\theta = \Delta\varphi/2$, as illustrated in Fig. 1(e). Therefore, by measuring the azimuth angle θ of the zero phase difference position, one can obtain the chiral phase difference between the incident wave's LCP and RCP components. The purpose of the circular disks in the images is to measure the chiral amplitude contrast of the incident light, as they indicate the intensities of the LCP and RCP components. By measuring the intensities on the disks, one can determine the handedness of the incident light (as well as the overall intensity of the incident beam). As any polarization state is a linear combination of LCP and RCP, the chiral phase difference and chiral amplitude contrast uniquely define the polarization state of the incident light.

3. THEORETICAL DESCRIPTION

The phase difference, namely, the zero phase difference angle $\theta = \Delta\varphi/2$, can be extracted by analyzing the field distribution along the ring, which is formed by interference. In terms of linearly polarized components, LCP and RCP can be expressed as $\mathbf{L} = \sqrt{2}/2[1 \quad -i]^T$ and $\mathbf{R} = \sqrt{2}/2[1 \quad i]^T$, respectively.
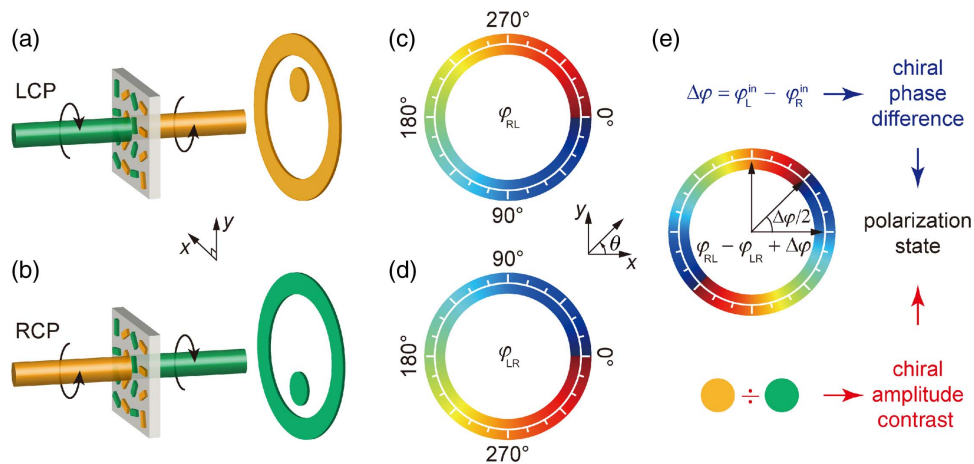
Fig. 1. Holographic polarimetry concept. (a), (b) Circular-polarization-dependent metahologram for generating RCP and LCP images of a ring containing an upper or lower circular disk under LCP and RCP illumination, respectively. (c), (d) For illustration of the working mechanism, helical phase distributions φ_{RL} and φ_{LR} with –1 and +1 topological charges are assigned to the holographic rings generated by LCP and RCP illumination, respectively. (e) Phase difference distribution $\varphi_{RL} - \varphi_{LR} + \Delta\varphi$, where $\Delta\varphi$ is the chiral phase difference between the incident LCP and RCP components of the light. By comparing the intensities of the top and bottom circular disks, the chiral amplitude contrast can be obtained. The polarization state can thus be determined by combining the chiral phase difference and chiral amplitude contrast.

In this circular polarization basis, any polarization state can be expressed as

$$\mathbf{P} = l_0 e^{i\varphi_L^{in}} \mathbf{L} + r_0 e^{i\varphi_R^{in}} \mathbf{R} = r_0 e^{i\varphi_R^{in}}[ae^{i\Delta\varphi}\mathbf{L} + \mathbf{R}], \quad (1)$$

where l_0 (φ_L^{in}) and r_0 (φ_R^{in}) represent the amplitudes (phases) of the incident LCP and RCP electric field with $l_0^2 + r_0^2 = 1$, while $a = l_0/r_0$ is the chiral amplitude contrast and $\Delta\varphi$ is the chiral phase difference between incident LCP and RCP with $a \in [0, \infty]$ and $\Delta\varphi \in [0, 360°]$. Applying the above definition to the generated cross-polarized holographic images, we obtain the polarization distribution **PD** along the ring as

$$\mathbf{PD}(\theta) = l_0 e^{i\varphi_L^{in}} e^{i\varphi_{RL}} \mathbf{R} + r_0 e^{i\varphi_R^{in}} e^{i\varphi_{LR}} \mathbf{L}$$
$$= \frac{\sqrt{2}}{2} e^{i(\varphi_{LR}+\varphi_R^{in})} \left\{ l_0 e^{i(\Delta\varphi-2\theta)} \begin{bmatrix} 1 \\ i \end{bmatrix} + r_0 \begin{bmatrix} 1 \\ -i \end{bmatrix} \right\}, \quad (2)$$

which is θ-dependent. While the intensity of light is uniform along the ring, interference modulates the intensity of any linearly polarized component along the ring. For example, the intensity distribution of the x-polarized component is given by

$$|PD_x(\theta)|^2 = \frac{1}{2}r_0^2 + \frac{1}{2}l_0^2 + l_0 r_0 \cos(2\theta - \Delta\varphi). \quad (3)$$

Equation (3) indicates that the intensity distribution of the x-polarized component is θ-dependent. At $\theta = \Delta\varphi/2$ (zero phase difference angle) and $\theta = \Delta\varphi/2 + 180°$, the intensity reaches its maxima, while it reaches minima at $\theta = \Delta\varphi/2 + 90°$ and $\theta = \Delta\varphi/2 + 270°$. Therefore, by measuring the azimuth angles of the maxima or minima, we can obtain the chiral phase difference $\Delta\varphi$. Another method to extract the chiral phase difference is to take the Fourier transform of Eq. (3), where the opposite phase value of the second Fourier order equals $\Delta\varphi$ (see Supplement 1, Section 1). In addition, the maximum and minimum intensities along the ring give some information

about the ratio between the amplitudes of the LCP and RCP components. In particular, the minimum intensity is zero for linearly polarized incident light, and the intensity modulation along the ring vanishes for circularly polarized incident light. However, this does not reveal the handedness of the incident wave as interchanged magnitudes of the two circular polarization components (with chiral amplitude contrast a and $1/a$) give rise to the same linearly polarized component of the intensity distribution on the ring. As such, an independent measurement is required to unambiguously determine the ratio a between the two circular polarization components. This is achieved by the measurement of the intensities of the two circular disks. According to Eq. (1), a and $\Delta\varphi$ uniquely identify the polarization of the incident light. It should be noted that the key in obtaining the chiral phase difference is the phase difference distribution between φ_{RL} and φ_{LR} in Fig. 1(e). The proposed method will still work if the same phase difference distribution is generated by phase distributions along the holographic rings that differ from those in Figs. 1(c) and 1(d).

4. NUMERICAL DEMONSTRATION OF HOLOGRAPHIC POLARIMETRY

To confirm the working mechanism, several examples are presented in Fig. 2. Figures 2(a)–2(d) illustrate the theoretical x-polarized components of the generated images for incident light of four different polarization states: RCP, +45° linear polarization, left-handed elliptical, and right-handed elliptical polarizations, respectively. Here, the two elliptical polarization states have the same orientation angles ψ and ellipticities χ of the same magnitude. The physical meanings of ψ and χ are schematically illustrated in Fig. 2(e). Under the RCP illumination, the x-polarized intensity distribution along the ring is uniform and only the lower circular disk appears. In the other three cases, the incident light contains both LCP and RCP components,
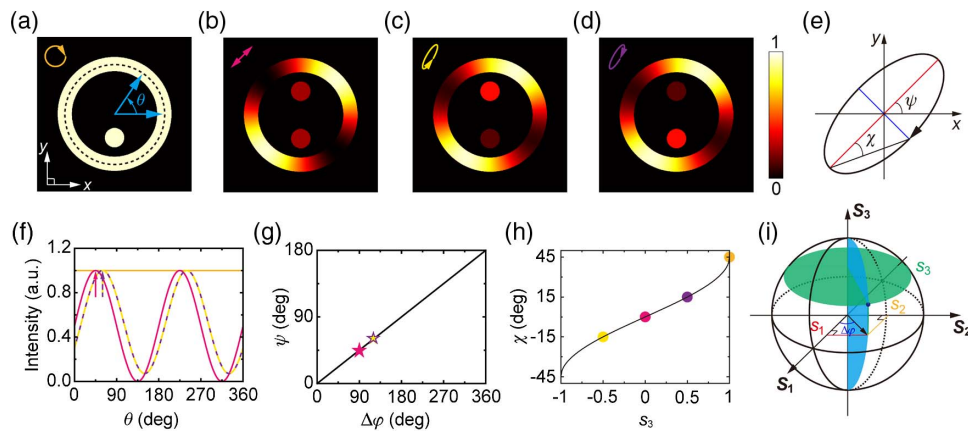
Fig. 2. Numerical demonstration of holographic polarimetry. (a)–(d) Ideal calculated x-polarized image components for illumination of the metahologram by waves with (a) RCP, (b) +45° linear, (c) left-handed elliptical, and (d) right-handed elliptical polarization, as indicated by the corresponding inset arrows. Here, the radial intensity distributions within the rings in (a)–(d) are uniform. (e) Schematic of a polarization ellipse, where ψ and χ represent the polarization orientation angle and ellipticity, respectively. For the four incident polarizations in (a)–(d), we set $(\psi, \chi) = $ (arbitrary value, 45°), (45°, 0°), (60°, –15°), and (60°, 15°), respectively. (f) Normalized intensity distributions along the rings (dashed circle in a) in (a)–(d) as a function of azimuth angle θ, respectively. The arrows point to the first maximum, whose θ corresponds to half of the chiral phase difference. (g), (h) Theoretical relationships between (g) polarization orientation angle as a function of chiral phase difference: $\psi = \Delta\varphi/2$, and (h) polarization ellipticity as a function of s_3 as defined in Eq. (4): $\chi = \text{atan}[s_3/(1 - s_3^2)^{1/2}]/2$, $s_3 \in [-1, 1]$. Here, $s_3 = -1$, 0, 1 (corresponding to $a = \infty$, 1, 0) represent LCP, linear polarization, RCP, respectively. The color markers in (g), (h) show the chiral phase difference and chiral amplitude contrast extracted from the holographic images in (a)–(d) using corresponding colors for markers and polarization arrows. (i) Schematic of a unit Poincaré sphere in 3D Cartesian coordinates formed by the Stokes parameters s_1, s_2, s_3. The green and blue circles are the s_3 latitude and $\Delta\varphi$ meridian on the sphere, whose intersection point represents the polarization state.

leading to a sinusoidal x-polarized intensity distribution along the ring caused by interference, and visibility of both circular disks with different intensity contrasts. The contrast is determined by the corresponding values of l_0 and r_0. Figure 2(f) shows the normalized intensity distribution along the ring [dashed circle illustrated in Fig. 2(a)]. These intensity curves can be fitted with $m + n \cos(2\theta - \Delta\varphi)$. The inset arrows in Fig. 2(f) point to the maxima of the curves, whose θ values correspond to half of the chiral phase differences.

Figures 2(g) and 2(h) illustrate the theoretical relationships between the polarization orientation angle and chiral phase difference, as well as polarization ellipticity and chiral amplitude contrast (defined in caption), respectively. From Figs. 2(a)–2(d), the corresponding chiral phase differences and chiral amplitude contrasts for the four incident polarizations can be extracted, except for the chiral phase difference under RCP illumination as no such phase difference can be defined for a circularly polarized wave. The chiral phase difference under the $+45°$ linearly polarized illumination is $90°$ while the chiral amplitude contrast is unity due to LCP and RCP components of equal intensity. The two elliptically polarized incident waves have the same x-polarized intensity distributions along the ring, meaning that they have the same chiral phase difference. However, the chiral amplitude contrast is different due to their opposite handednesses. These extracted values of chiral phase difference and chiral amplitude contrast identify the corresponding polarization orientation angles and ellipticities uniquely, as indicated in Figs. 2(g) and 2(h). They are in excellent agreement with theoretical settings, revealing the hologram's ability of distinguishing polarization states.

5. EXTRACTION OF THE STOKES PARAMETERS

Besides polarization orientation angle and ellipticity, the Stokes parameters can also be extracted from the holographic images to characterize the incident polarization state. The Stokes parameters (s_0, s_1, s_2, s_3) are a set of values commonly used to characterize polarization states, where s_0 is proportional to the light intensity, s_1, s_2, and s_3 form a three-dimensional (3D) vector $\mathbf{s} = s_1\mathbf{S_1} + s_2\mathbf{S_2} + s_3\mathbf{S_3}$ describing the polarization state, and $s_1^2 + s_2^2 + s_3^2 = ps_0^2$ with $p \in [0, 1]$ representing the degree of polarization. For fully polarized light ($p = 1$), the vector (s_1, s_2, s_3) that is normalized to s_0 forms a unit sphere in 3D Cartesian coordinates, which is the so-called Poincaré sphere, as illustrated in Fig. 2(i). Each point on this sphere represents a certain polarization state. Conventionally, determining the Stokes parameters requires a series of power measurement followed by solving complicated equations. Here, we show that polarization measurements in the circular polarization basis greatly simplify the process.

First, by measuring the intensities of the upper and lower circular disks within the ring, I_L and I_R, respectively, we can obtain the value of s_3 by [53]

$$s_3 = \frac{I_R - I_L}{I_R + I_L} = \frac{1 - a^2}{1 + a^2}. \tag{4}$$

For fully polarized light, $s_1^2 + s_2^2 = 1 - s_3^2$, and we only need to determine the remaining Stokes parameters in the s_3 latitude on the sphere, as indicated by the edge of the green circle in Fig. 2(i). Next, by analyzing the x-polarized intensity distribution along the ring, we can obtain the chiral phase difference $\Delta\varphi$, which corresponds to the half-meridian on the sphere, as

indicated by the edge of the blue circle in Fig. 2(i). As such, the Stokes parameters of the incident light are uniquely determined by the intersection point of the latitude and meridian on the Poincaré sphere, as indicated by the black point in Fig. 2(i). The remaining Stokes parameters can be easily obtained through

$$s_1 = \sqrt{1 - s_3^2} \cos \Delta\varphi, \tag{5}$$

$$s_2 = \sqrt{1 - s_3^2} \sin \Delta\varphi. \tag{6}$$

6. DESIGN OF THE METAHOLOGRAM

Above, we have described a holographic method for polarization state characterization. Next we design a metasurface with the above functionalities using the PB phase method and a modified Gerchberg–Saxton (GS) algorithm (see Supplement 1, Section 2). For simplicity, we use a single-layer plasmonic metasurface made up of identical gold bar resonators with different orientations operating in the near-infrared regime. Such a metasurface is well-suited for our proof-of-principle demonstration, but it is not very efficient [58,59]. Higher efficiency can be achieved with metasurfaces that are composed of multilayer plasmonic structures or dielectric structures [60]. Figures 3(a) and 3(b) show the designed target holographic images for LCP and RCP illumination, respectively. In order to spatially separate the ring and disk patterns from the metasurface's brighter zero-order transmitted output (at the center of the holographic image) and to avoid cross talk due to the twin images generated by the reversed LCP and RCP illuminations, we place the target ring and disk patterns in the left-top corner of the holographic images. Since the twin images generated by the PB phase metasurfaces are centrosymmetric and phase conjugate to the designed holographic images [37], the corresponding twin ring and disk patterns will appear in the right-bottom corner of the final holographic images with opposite phase distributions along the rings. As the twin patterns are not overlapped with the target ones, they will have no influence to the polarization measurement. Actually, the twin patterns can also be applied in measuring the polarization state. Details about the twin images can be seen in Supplement 1, Section 3. By applying a modified GS algorithm, where the phase relation between the two holographic images is taken into account, the corresponding phase distributions for generating these two images are obtained, as illustrated in Figs. 3(c) and 3(d), respectively. Before that, a precompensation algorithm is applied in order to avoid pattern distortion at the design wavelength when directly projecting the generated images to the far-field [35,37]. Like many other pure-phase-type holograms based on such iteration, the proposed modified algorithm cannot control the phase distributions of the two holographic images either. Though it cannot make the final phase distributions of the rings identical to those shown in Figs. 1(c) and 1(d), it can guarantee that the phase difference distribution is as shown in Fig. 1(e), which is sufficient for identifying the chiral phase difference based on the above-mentioned method (see Supplement 1, Sections 2 and 3). Here, the phase distributions in Figs. 1(c) and 1(d) are plotted to provide a simple explanation of the working mechanism. Such phase distributions would result from projection of circu-
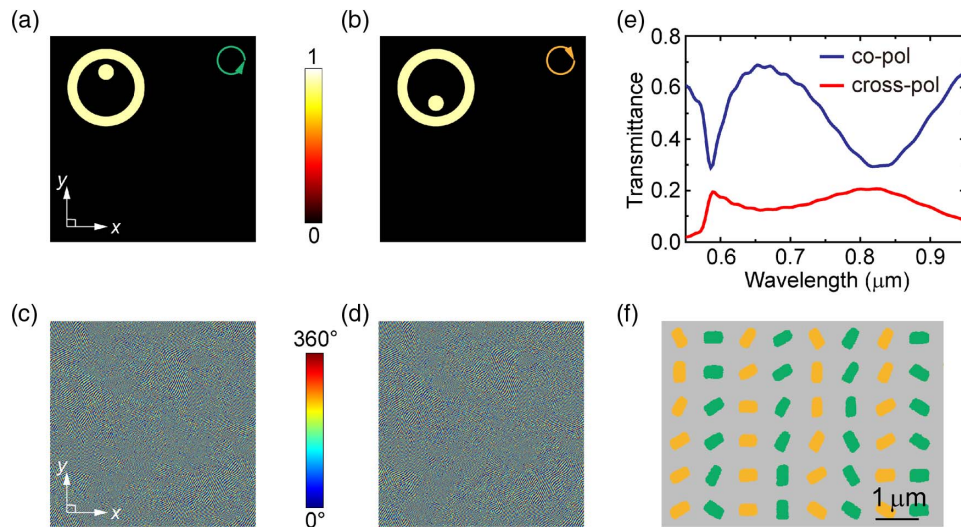
Fig. 3. Metahologram design for broadband polarimetry. (a), (b) Designed holographic images generated under the LCP and RCP illumination, respectively, where the target ring and disk patterns are placed in the left-top corners. (c), (d) The corresponding calculated phase distributions of the holograms for LCP and RCP illumination based on the modified Gerchberg–Saxton algorithm, respectively. (e) Simulated copolarized and cross-polarized transmittance spectra of the metasurface's bar resonators in the circular polarization basis. (f) Scanning electron microscopy image of a part of the fabricated metahologram, where resonators generating the holograms in panels (a) and (b) are colored green and orange, respectively.

larly polarized positive first-order and negative first-order vortex beams of opposite handedness through a ring aperture.

Here, the phase distributions are designed to generate images that cover a wide angular range of 60° × 60° under normal illumination at 800 nm wavelength. To assimilate the two phase distributions into one metasurface, the following multiplexing method is used [36,37,43,44]. The basic unit cell of the metasurface is a bar resonator on a quartz substrate, which is made of gold with a length of 200 nm, a width of 100 nm, a thickness of 45 nm, and a period of 400 nm, respectively. Bar resonators for generating different holograms are highlighted green and orange in Fig. 3(f). The orientation angle distribution of the bar resonators in the metasurface is designed using the PB phase method: orientation angles of green bars equal 1/2 times the phase distribution in Fig. 3(c) for generating the RCP image of Fig. 3(a) under the LCP illumination, while orientation angles of orange bars equal –1/2 times the phase distribution in Fig. 3(d) for generating the LCP image of Fig. 3(b) under the RCP illumination. Here, to simplify the design, eight phase levels (thus eight bar orientations) are applied. The metasurface covers an area of 355.2 μm × 355.2 μm and contains 888 × 888 resonators.

The PB phase is wavelength-independent; however, the efficiency of circular polarization conversion that controls the hologram's brightness is wavelength-dependent and therefore determines the spectral band in which the metasurface can operate. This cross-polarization generation efficiency is determined by the anisotropic resonant response of the unit cell. Figure 3(e) shows the simulated circular transmittance spectra of the bar resonators (normalized to the transmittance of the bare substrate), which have resonances at 586 and 828 nm, corresponding to the eigen resonance modes along the width and length of the bars, respectively. The corresponding eigen transmittance spectra and resonance behaviors of the two modes are illustrated in Supplement 1, Section 4. In the simulations, quartz is modeled with a refractive index of 1.45, while gold is described by a Drude model with plasma frequency $\omega_p = 1.366 \times 10^{16}$ rad/s and

collision frequency $\gamma = 1.2 \times 10^{14}$ rad/s. Based on the full width at half-maximum of the cross-polarized transmittance spectrum, this results in a broadband metahologram operating in the 580–940 nm wavelength range.

7. EXPERIMENTAL CHARACTERIZATION

To experimentally characterize the performance of our design, the metahologram was fabricated on a quartz substrate using electron beam lithography, with subsequent deposition of 5 nm chromium as an adhesion layer and 40 nm gold, followed by a lift-off process. Details about the fabrication process can be seen in Supplement 1, Section 5. Figure 3(f) shows a false color scanning electron microscopy image of a small part of the fabricated metahologram, where the green and orange bar resonators generate the images in Figs. 3(a) and 3(b), respectively. Though the fabricated bar resonators show variable geometric parameters, the presented metasurface also shows good performance. Simple, preliminary measurements on the metasurface confirm that incident LCP and RCP generate the desired holographic images and that their superposition yields the intended phase difference distribution along the ring (see Supplement 1, Section 6). We have also theoretically studied the generated holographic images of the metahologram with different levels of amplitude and phase noises. The dimension of the rings and disks, as well as the phase difference distribution along the ring, are very stable as the noise level increases, indicating a large fabrication tolerance of the presented design (see Supplement 1, Section 7). Here, we concentrate on fine measurements on the metasurface that verify its suitability for polarization analysis. Figure 4(a) schematically illustrates the corresponding experimental setup. A continuous wave Ti:sapphire laser with a wavelength of 798 nm was used as the light source. A linear polarizer (LP1) was used to initialize the polarization to x-polarized light. A wave plate (WP), either half-wave plate or quarter-wave plate, was then used to generate light with known polarization states to be measured and
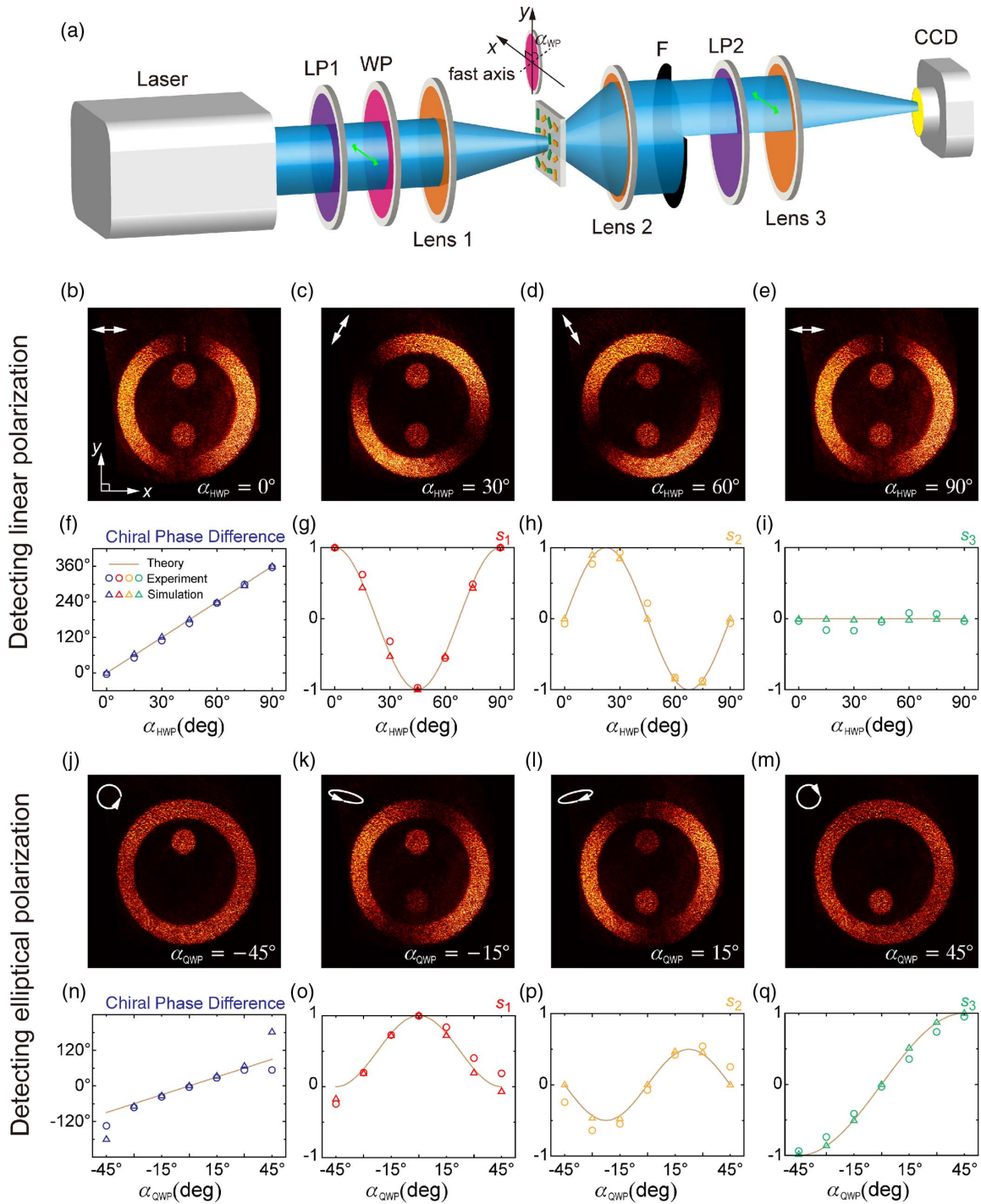
Fig. 4. Experimental demonstration of holographic polarimetry. (a) Schematic of the experimental setup. LP, linear polarizer; WP, wave plate; F, space filter. Green arrows indicate the polarization state after LP1 and LP2. The orientation angle of wave plate's fast axis is measured from the positive y axis, increasing towards the negative x axis as illustrated by the inset. (b)–(e), (j)–(m) Holographic images captured by the CCD camera for orientation angles of the half-wave plate's fast axis of $\alpha_{HWP} = 0°$, 30°, 60°, 90°, and orientation angles of the quarter-wave plate's fast axis of $\alpha_{QWP} = -45°$, -15°, 15°, 45°, respectively. The inset arrows schematically indicate the corresponding theoretical polarization state. (f), (n) Theoretical, experimental, and simulated chiral phase differences when rotating the half-wave plate and the quarter-wave plate, respectively. (g)–(i), (o)–(q) Theoretical, experimental, and simulated Stokes parameters s_1, s_2, and s_3 when rotating the half-wave plate and the quarter-wave plate, respectively.

compared. Lens 1 was used to normally focus the light onto the metasurface. Lens 2 was used to collect the diffracted light from the metasurface, which actually functioned as a space Fourier-transforming device. A space filter (F) was placed behind to block the zero-order output and the conjugate image. Then, a second

linear polarizer (LP2) was used to select the x-polarized component. Following that, lens 3 was used to project the holographic image onto a CCD camera.

We first used a half-wave plate to control the polarization incident on the metasurface. The orientation angle α_{HWP} of the

wave plate's fast axis was gradually changed from 0° to 90° in 15° steps, generating linear polarization with an electric field orientation that rotates from x to y and then to $-x$ in 30° steps. Figures 4(b)–4(e) illustrate the measured holographic ring and disk patterns for $\alpha_{\mathrm{HWP}} = 0°$, 30°, 60°, and 90°, respectively. Figure 4(f) illustrates the chiral phase difference as a function of α_{HWP}. Here, due to the influence from the zero-order output and background noise, as well as the low angle resolution, we extracted the chiral phase difference not by finding the x-polarized intensity maxima, but using the above-mentioned Fourier transform method to get a better accuracy, in which the whole measured x-polarized intensity distribution along the ring is taken into account. Here, to enhance the signal-to-noise ratio of the intensity distribution along the ring, we integrated the intensities over the ring width at each azimuth angle. It can be seen that the measured results agree well with theoretical calculations. To extract the Stokes parameters, we first calculated s_3 using Eq. (4). I_L and I_R were calculated by integrating the intensities over a fixed-size area in the corresponding circular disk regions, followed by background noise subtraction for improved accuracy. The background noise was determined by intensity integration over a disk-sized area at the center of the ring. Then, s_1 and s_2 were obtained by using Eqs. (5) and (6), respectively. Details about the extraction method of the chiral phase difference and the Stokes parameters can be seen in Supplement 1, Section 8. Figures 4(g)–4(i) illustrate the extracted Stokes parameters as a function of α_{HWP}, where very good agreement with theoretical calculations is achieved. We also applied a quarter-wave plate to control the incident polarization. The orientation angle α_{QWP} of the quarter-wave plate's fast axis was gradually changed from $-45°$ to 45° in steps of 15°, corresponding to a gradual polarization change from LCP to x polarization and then to RCP. Figures 4(j)–4(m) show the measured holographic images at $\alpha_{\mathrm{QWP}} = -45°$, $-15°$, 15° and 45°, respectively. Figure 4(n) shows the chiral phase difference, while Figs. 4(o)–4(q) illustrate the extracted Stokes parameters, which also agree well with theoretical calculations. We note that the chiral phase difference becomes undefined for pure circular polarizations, which should be expected to result in detection of random circular phase differences by an ideal polarimeter. This explains the apparent, but meaningless, differences between measured/simulated and theoretical chiral phase differences around $\alpha_{\mathrm{QWP}} = -45°$ and 45°, which are induced by minor nonuniformities in the intensity distribution along the ring [see Figs. 4(j) and 4(m), as well as Figs. S3(a) and S3(b)], since the amplitude of the interference-induced periodic variation along the ring is very small (l_0 or r_0 approaches 0), as indicated by Eq. (3). When the amplitude becomes comparable to the noise level, the discrepancies between the extracted and theoretical chiral phase difference become large. However, such effect can be reduced by using a metahologram with higher efficiency. Overall, the main sources of measurement inaccuracies are the intensity of the transmitted zero-order beam, background noise, rotation errors of polarization optics, and phase inaccuracies of the wave plates. Figure 4 also shows simulated chiral phase differences and Stokes parameters, which are free from the above sources of experimental errors, resulting in excellent agreement with theory.

8. DISCUSSION AND CONCLUSION

Many applications depend on polarization state characterization with a minimum error. The holographic method demonstrated here still has much room for optimization. The accuracy of phase difference measurements can be improved by applying phase-control structures with higher efficiency [60]. Measurements of the chiral amplitude contrast or s_3 are affected by the background noise, which is commonly uniformly distributed. This can be improved by increasing the circular disk intensities relative to the ring intensity. The phase difference between LCP and RCP light components is designed to be proportional to -2θ along the ring, resulting in only two periods of intensity oscillation for the linearly polarized detected light. We can increase the topological charge of $\varphi_{\mathrm{RL}} - \varphi_{\mathrm{LR}}$, which effectively increases the sampling frequency and allows extraction of the chiral phase difference with better accuracy. We have also theoretically designed a metahologram based on the above optimization method, and corresponding simulations show a much improved polarization accuracy. While we used the x-polarized output component to extract the chiral phase difference, we note that any linearly polarized component could be used. When detecting another linear polarization, twice the orientation angle of the linear polarizer needs to be subtracted from the measured phase difference to achieve the final chiral phase difference. This also allows for easy calibration of the device, even if the linear polarizer behind the metasurface is not precisely adjusted.

It should be mentioned that, when the incident wavelength deviates from the design wavelength of 800 nm, the size of the ring and disk patterns will scale proportional to the wavelength [42]. Besides, there will also be angular distortions to the patterns, resulting in rings and disks that will no longer be perfectly circular. A larger wavelength deviation will result in larger distortions. Even though this will introduce an additional error in the extraction of the chiral phase difference, both simulated and experimental results at wavelengths from 650 to 900 nm show that the holographic images still allow extraction of the polarization state with good accuracy, indicating broadband and robust operation of the presented metahologram (see Supplement 1, Section 9). To avoid such distortion, one could improve the design by placing the pattern in the center of the holographic image using efficient metasurfaces (see Supplement 1, Section 10). Besides fully polarized light, our metahologram also has potential for characterization of partially polarized light (see Supplement 1, Section 11). However, it is not suitable for characterization of vector beams, since it will generate a superposition of images corresponding to all local polarization states of the vector beam.

In conclusion, we demonstrated an effective holographic method for broadband polarization detection based on a metasurface that generates overlapping circular-polarization-dependent images with a predesigned phase difference distribution. Use of the PB phase method, which exploits the orientation of anisotropic elements, makes the metasurface inherently broadband and tolerant to fabrication inaccuracies. The corresponding measured efficiencies of the designed proof-of-principle metasurface for the patterns at the left-top corners are only 0.05% at 650 nm, 0.23% at 800 nm, and 0.17% at 850 nm wavelength, respectively. Though the efficiency is quite low, as long as the holographic image can be captured, the metahologram could work well for polarization measurements, irrespective of the intensity of the incident light. Such holographic metasurfaces could enable very compact polarimeters without moving parts that detect polarization in a single step. Further compactness can be achieved by fabricating the linear polarizer (e.g., a metal grid

or nanoparticles) on the backside of the metasurface substrate. Importantly, the modified GS algorithm, which we developed to generate the phase difference distribution, can also be used to design arbitrary holographic images with any desired polarization distribution, e.g., for polarization encoding of secret information, depolarization, and 3D displays. The data for this paper can be obtained from the University of Southampton ePrints research repository [61].

See Supplement 1 for supporting content.

REFERENCES

1. M. Born and E. Wolf, *Principles of Optics*, 7th ed. (Cambridge University, 1999).
2. D. S. Kliger, J. M. Lewis, and C. E. Randall, *Polarized Light in Optics and Spectroscopy* (Academic, 1990).
3. J. S. Tyo, D. L. Goldstein, D. B. Chenault, and J. A. Shaw, "Review of passive imaging polarimetry for remote sensing applications," Appl. Opt. **45**, 5453–5469 (2006).
4. J. N. Damask, *Polarization Optics in Telecommunications* (Springer, 2005).
5. C. H. Bennett and D. P. DiVincenzo, "Quantum information and computation," Nature **404**, 247–255 (2000).
6. R. M. A. Azzam and N. M. Bashara, *Ellipsometry and Polarized Light* (North-Holland, 1977).
7. A. Rodger and B. Nordén, *Circular Dichroism and Linear Dichroism* (Oxford University, 1997).
8. H. G. Berry, G. Gabrielse, and A. E. Livingston, "Measurement of the Stokes parameters of light," Appl. Opt. **16**, 3200–3205 (1977).
9. R. M. A. Azzam, "Division-of-amplitude photopolarimeter (DOAP) for the simultaneous measurement of all four Stokes parameters of light," Opt. Acta **29**, 685–689 (1982).
10. N. Yu, P. Genevet, M. A. Kats, F. Aieta, J.-P. Tetienne, F. Capasso, and Z. Gaburro, "Light propagation with phase discontinuities: generalized laws of reflection and refraction," Science **334**, 333–337 (2011).
11. N. Yu and F. Capasso, "Flat optics with designer metasurfaces," Nat. Mater. **13**, 139–150 (2014).
12. H.-T. Chen, A. J. Taylor, and N. Yu, "A review of metasurfaces: physics and applications," Rep. Prog. Phys. **79**, 076401 (2016).
13. P. Genevet, F. Capasso, F. Aieta, M. Khorasaninejad, and R. Devlin, "Recent advances in planar optics: from plasmonic to dielectric metasurfaces," Optica **4**, 139–152 (2017).
14. L. Huang, X. Chen, H. Mühlenbernd, G. Li, B. Bai, Q. Tan, G. Jin, T. Zentgraf, and S. Zhang, "Dispersionless phase discontinuities for controlling light propagation," Nano Lett. **12**, 5750–5755 (2012).
15. S. Sun, K.-Y. Yang, C.-M. Wang, T.-K. Juan, W. T. Chen, C. Y. Liao, Q. He, S. Xiao, W.-T. Kung, G.-Y. Guo, L. Zhou, and D. P. Tsai, "High-efficiency broadband anomalous reflection by gradient metasurfaces," Nano Lett. **12**, 6223–6229 (2012).
16. X. Zhang, Z. Tian, W. Yue, J. Gu, S. Zhang, J. Han, and W. Zhang, "Broadband terahertz wave deflections based on C-shape complex metamaterials with phase discontinuities," Adv. Mater. **25**, 4567–4572 (2013).
17. H. Zhang, M. Kang, X. Zhang, W. Guo, C. Lv, Y. Li, W. Zhang, and J. Han, "Coherent control of optical spin-to-orbital angular momentum conversion in metasurface," Adv. Mater. **29**, 1604252 (2017).
18. L. Cong, Y. K. Srivastava, H. Zhang, X. Zhang, J. Han, and R. Singh, "All-optical active THz metasurfaces for ultrafast polarization switching and dynamic beam splitting," Light Sci. Appl. **7**, 28 (2018).
19. X. Chen, L. Huang, H. Mühlenbernd, G. Li, B. Bai, Q. Tan, G. Jin, C.-W. Qiu, S. Zhang, and T. Zentgraf, "Dual-polarity plasmonic metalens for visible light," Nat. Commun. **3**, 1198 (2012).
20. A. Arbabi, Y. Horie, A. J. Ball, M. Bagheri, and A. Faraon, "Subwavelength-thick lenses with high numerical apertures and large efficiency based on high-contrast transmitarrays," Nat. Commun. **6**, 7069 (2015).
21. E. Arbabi, A. Arbabi, S. M. Kamali, Y. Horie, and A. Faraon, "Controlling the sign of chromatic dispersion in diffractive optics with dielectric metasurfaces," Optica **4**, 625–632 (2017).
22. S. Wang, P. C. Wu, V.-C. Su, Y.-C. Lai, C. H. Chu, J.-W. Chen, S.-H. Lu, J. Chen, B. Xu, C.-H. Kuan, T. Li, S. Zhu, and D. P. Tsai, "Broadband achromatic optical metasurface devices," Nat. Commun. **8**, 187 (2017).
23. E. Maguid, I. Yulevich, D. Veksler, V. Kleiner, M. L. Brongersma, and E. Hasman, "Photonic spin-controlled multifunctional shared-aperture antenna array," Science **352**, 1202–1206 (2016).
24. W. T. Chen, M. Khorasaninejad, A. Y. Zhu, J. Oh, R. C. Devlin, A. Zaidi, and F. Capasso, "Generation of wavelength-independent subwavelength Bessel beams using metasurfaces," Light Sci. Appl. **6**, e16259 (2017).
25. H. Zhang, X. Zhang, Q. Xu, Q. Wang, Y. Xu, M. Wei, Y. Li, J. Gu, Z. Tian, C. Ouyang, X. Zhang, C. Hu, J. Han, and W. Zhang, "Polarization-independent all-silicon dielectric metasurfaces in the terahertz regime," Photon. Res. **6**, 24–29 (2018).
26. S. Sun, Q. He, S. Xiao, Q. Xu, X. Li, and L. Zhou, "Gradient-index metasurfaces as a bridge linking propagating waves and surface waves," Nat. Mater. **11**, 426–431 (2012).
27. L. Huang, X. Chen, B. Bai, Q. Tan, G. Jin, T. Zentgraf, and S. Zhang, "Helicity dependent directional surface plasmon polariton excitation using a metasurface with interfacial phase discontinuity," Light Sci. Appl. **2**, e70 (2013).
28. X. Zhang, Y. Xu, W. Yue, Z. Tian, J. Gu, Y. Li, R. Singh, S. Zhang, J. Han, and W. Zhang, "Anomalous surface wave launching by handedness phase control," Adv. Mater. **27**, 7123–7129 (2015).
29. L. Huang, X. Chen, H. Mühlenbernd, H. Zhang, S. Chen, B. Bai, Q. Tan, G. Jin, K.-W. Cheah, C.-W. Qiu, J. Li, T. Zentgraf, and S. Zhang, "Three-dimensional optical holography using a plasmonic metasurface," Nat. Commun. **4**, 2808 (2013).
30. X. Ni, A. V. Kildishev, and V. M. Shalaev, "Metasurface holograms for visible light," Nat. Commun. **4**, 2807 (2013).
31. W. Wan, J. Gao, and X. Yang, "Metasurface holograms for holographic imaging," Adv. Opt. Mater. **5**, 1700541 (2017).
32. L. Huang, S. Zhang, and T. Zentgraf, "Metasurface holography: from fundamentals to applications," Nanophotonics **7**, 1169–1190 (2018).
33. Y. Montelongo, J. O. Tenorio-Pearl, W. I. Milne, and T. D. Wilkinson, "Polarization switchable diffraction based on subwavelength plasmonic nanoantennas," Nano Lett. **14**, 294–298 (2014).
34. Y. Yifat, M. Eitan, Z. Iluz, Y. Hanein, A. Boag, and J. Scheuer, "Highly efficient and broadband wide-angle holography using patch-dipole nanoantenna reflectarrays," Nano Lett. **14**, 2485–2490 (2014).
35. G. Zheng, H. Mühlenbernd, M. Kenney, G. Li, T. Zentgraf, and S. Zhang, "Metasurface holograms reaching 80% efficiency," Nat. Nanotechnol. **10**, 308–312 (2015).
36. W. T. Chen, K.-Y. Yang, C.-M. Wang, Y.-W. Huang, G. Sun, I.-D. Chiang, C. Y. Liao, W.-L. Hsu, H. T. Lin, S. Sun, L. Zhou, A. Q. Liu, and D. P. Tsai, "High-efficiency broadband meta-hologram with polarization-controlled dual images," Nano Lett. **14**, 225–230 (2014).
37. D. Wen, F. Yue, G. Li, G. Zheng, K. Chan, S. Chen, M. Chen, K. F. Li, P. W. H. Wong, K. W. Cheah, E. Y. B. Pun, S. Zhang, and X. Chen, "Helicity multiplexed broadband metasurface holograms," Nat. Commun. **6**, 8241 (2015).
38. Z. Xie, T. Lei, G. Si, X. Wang, J. Lin, C. Min, and X. Yuan, "Meta-holograms with full parameter control of wavefront over a 1000 nm bandwidth," ACS Photon. **4**, 2158–2164 (2017).
39. J. P. B. Mueller, N. A. Rubin, R. C. Devlin, B. Groever, and F. Capasso, "Metasurface polarization optics: independent phase control of arbitrary orthogonal states of polarization," Phys. Rev. Lett. **118**, 113901 (2017).
40. S. Xiao, F. Zhong, H. Liu, S. Zhu, and J. Li, "Flexible coherent control of plasmonic spin-Hall effect," Nat. Commun. **6**, 8360 (2015).
41. Q. Xu, X. Zhang, Y. Xu, C. Ouyang, Z. Tian, J. Gu, J. Li, S. Zhang, J. Han, and W. Zhang, "Polarization-controlled surface plasmon holography," Laser Photon. Rev. **11**, 1600212 (2017).

42. X. Li, L. Chen, Y. Li, X. Zhang, M. Pu, Z. Zhao, X. Ma, Y. Wang, M. Hong, and X. Luo, "Multicolor 3D meta-holography by broadband plasmonic modulation," Sci. Adv. **2**, e1601102 (2016).

43. Q. Wang, E. Plum, Q. Yang, X. Zhang, Q. Xu, Y. Xu, J. Han, and W. Zhang, "Reflective chiral meta-holography: multiplexing holograms for circularly polarized waves," Light Sci. Appl. **7**, 25 (2018).

44. Y. Chen, X. Yang, and J. Gao, "Spin-controlled wavefront shaping with plasmonic chiral geometric metasurfaces," Light Sci. Appl. **7**, 84 (2018).

45. L. Cong, P. Pitchappa, N. Wang, and R. Singh, "Electrically programmable terahertz diatomic metamolecules for chiral optical control," Research **2019**, 7084251 (2019).

46. Z.-L. Deng, J. Deng, X. Zhuang, S. Wang, T. Shi, G. P. Wang, Y. Wang, J. Xu, Y. Cao, X. Wang, X. Cheng, G. Li, and X. Li, "Facile metagrating holograms with broadband and extreme angle tolerance," Light Sci. Appl. **7**, 78 (2018).

47. Z.-L. Deng, J. Deng, X. Zhuang, S. Wang, K. Li, Y. Wang, Y. Chi, X. Ye, J. Xu, G. P. Wang, R. Zhao, X. Wang, Y. Cao, X. Cheng, G. Li, and X. Li, "Diatomic metasurface for vectorial holography," Nano Lett. **18**, 2885–2892 (2018).

48. L. Cong, P. Pitchappa, Y. Wu, L. Ke, C. Lee, N. Singh, H. Yang, and R. Singh, "Active multifunctional microelectromechanical system metadevices: applications in polarization control, wavefront deflection, and holograms," Adv. Opt. Mater. **5**, 1600716 (2017).

49. L. Li, T. J. Cui, W. Ji, S. Liu, J. Ding, X. Wan, Y. B. Li, M. Jiang, C.-W. Qiu, and S. Zhang, "Electromagnetic reprogrammable coding-metasurface holograms," Nat. Commun. **8**, 197 (2017).

50. H.-C. Liu, B. Yang, Q. Guo, J. Shi, C. Guan, G. Zheng, H. Mühlenbernd, G. Li, T. Zentgraf, and S. Zhang, "Single-pixel computational ghost imaging with helicity-dependent metasurface hologram," Sci. Adv. **3**, e1701477 (2017).

51. J. Li, S. Kamin, G. Zheng, F. Neubrech, S. Zhang, and N. Liu, "Addressable metasurfaces for dynamic holography and optical information encryption," Sci. Adv. **4**, eaar6768 (2018).

52. F. Afshinmanesh, J. S. White, W. Cai, and M. L. Brongersma, "Measurement of the polarization state of light using an integrated plasmonic polarimeter," Nanophotonics **1**, 125–129 (2012).

53. A. Pors, M. G. Nielsen, and S. I. Bozhevolnyi, "Plasmonic metagratings for simultaneous determination of Stokes parameters," Optica **2**, 716–723 (2015).

54. A. Pors and S. I. Bozhevolnyi, "Waveguide metacouplers for in-plane polarimetry," Phys. Rev. Appl. **5**, 064015 (2016).

55. J. P. B. Mueller, K. Leosson, and F. Capasso, "Ultracompact metasurface in-line polarimeter," Optica **3**, 42–47 (2016).

56. S. Wei, Z. Yang, and M. Zhao, "Design of ultracompact polarimeters based on dielectric metasurfaces," Opt. Lett. **42**, 1580–1583 (2017).

57. P. C. Wu, J.-W. Chen, C.-W. Yin, Y.-C. Lai, T. L. Chung, C. Y. Liao, B. H. Chen, K.-W. Lee, C.-J. Chuang, C.-M. Wang, and D. P. Tsai, "Visible metasurfaces for on-chip polarimetry," ACS Photon. **5**, 2568–2573 (2018).

58. F. Monticone, N. M. Estakhri, and A. Alù, "Full control of nanoscale optical transmission with a composite metascreen," Phys. Rev. Lett. **110**, 203903 (2013).

59. A. Arbabi and A. Faraon, "Fundamental limits of ultrathin metasurfaces," Sci. Rep. **7**, 43722 (2017).

60. Q. He, S. Sun, S. Xiao, and L. Zhou, "High-efficiency metasurfaces: principles, realizations, and applications," Adv. Opt. Mater. **6**, 1800415 (2018).

61. University of Southampton ePrints research repository, https://doi.org/10.5258/SOTON/D0706.